Study of Microsegregation Buildup during Solidification of Spheroidal Graphite Cast Iron

CHRISTOPHE SELIG and JACQUES LACAZE

This work presents an attempt to describe the complex relationship between the development of the solidification microstructures and buildup of microsegregation in spheroidal graphite (SG) cast irons by coupling an experimental investigation and a modeling approach. Experimental characterization of microsegregation in cast iron was made by means of point counting microanalysis along a grid. With this method, the differences of silicon distribution in alloys solidified in the stable system, the metastable system, or in both systems were clearly evidenced. The distribution of manganese in alloy solidified in the stable system was also investigated. It has been, in particular, observed that alloys solidified in the stable (respectively, metastable) system present significant negative (respectively, positive) segregation of silicon, and that alloys solidified in both systems are much less segregated. The solidification path of these alloys has been conveniently reproduced by means of predictions made with a physical model accounting for the nature of the alloy, either hypoeutectic or hypereutectic, and for the sensitivity to temperature and composition of the partition coefficient of alloying elements.

I. INTRODUCTION

CHEMICAL heterogeneities, which build up during solidification of cast irons at the scale of the solidification microstructure (microsegregations), have been investigated for a long time because of their influence on the properties of cast products.[1–11] Microsegregations affect the microstructure resulting from the solidification step, namely, the gray (stable) to white (metastable) eutectic transition, but also the solid-state transformations during cooling or heat treatments. Charbonnier and Margerie[1,2] have shown that elements that favor the stable system such as silicon, nickel, or copper segregate negatively during stable solidification. The reverse is true for elements that favor the metastable system such as chromium and manganese, which segregate positively during stable solidification. Other authors[3–10] agree on these general features. It is worth emphasizing that Charbonnier and Margerie noted similar results for both lamellar and spheroidal graphite cast irons, and it is accepted that the segregation behavior of alloying elements is the same in gray and nodular cast irons. In irons that solidified in the metastable system, it has been found that segregation of chromium and silicon is inverted with respect to the case of stable solidification, while manganese segregates positively for both gray and white solidification.[1]

While the sign of the solidification segregation of the main alloying elements of cast irons is well established, there are a number of controversial features that need further investigation. Concerning stable solidification, studies on the role of the cooling rate and of cell or nodule count on the amplitude of microsegregation led to contradictory results. Concerning white solidification, positive segregation of silicon during the proeutectic deposit of austenite has been reported,[2,11] which could not be clearly understood. Also, Charbonnier and Margerie[2] observed that segregation is slightly less marked in as-cast malleable irons, but Feest *et al.*[12] found high positive segregation of silicon in white cast iron. In this line of studies, this work presents an attempt to describe the complex relationship between the development of the solidification microstructures and buildup of microsegregation in spheroidal graphite (SG) cast irons by coupling an experimental investigation and a modeling approach.

In most of the works devoted to the characterization of microsegregations, solute distribution was studied by means of microprobe measurements made either in selected areas or along line scans. Using the possibilities of automatic analysis, Feest *et al.*[12] characterized the silicon segregation in white and gray cast irons by use of a multipoint microprobe analysis. Provided the investigated area is large enough, one may consider that the features encountered are similar to those found in a random plane to cut through the structure. This method is then an effective means to get a statistically significant characterization of the distribution of alloying elements as discussed previously.[13,14] In the first part of this article, this method is to be applied to the study of the distribution of alloying elements in SG cast irons solidified in the stable, in the metastable, or in both systems.

In spite of the importance of microsegregations of alloying elements, only a limited number of works attempted to describe the formation of the microstructure and the kinetics of solidification together with the development of microsegregations in either lamellar or nodular graphite cast irons.[15–19] These models were limited to fully eutectic alloys, *i.e.*, they did not account for proeutectic deposits. Moreover, the partition coefficient of alloying elements, and particularly of silicon, was considered either as constant or, at best, values along the nearly isothermal equilibrium eutectic valley were used, which were most often taken from the works by Kagawa and Okamoto.[20] In the present work, the extension to multicomponent alloys of a model previously developed[21] to describe the solidification of hypereutectic as well as hypoeutectic spheroidal graphite cast

CHRISTOPHE SELIG, formerly Graduate Student, School of Mines, Nancy, France, 54042, is with the Branche Alliages Légers, VALFON, 01602 Trévous Cedex, France. JACQUES LACAZE, Senior Scientist, is with the Laboratoire Interfaces et Matériaux, Centre Inter-Universitaire de Recherche et Ingéniere des Matériaux (CIRIMAT), 31077 Toulouse Cedex 4, France.

Manuscript submitted September 2, 1999.

Table I. Nominal Composition of the Alloys Investigated

Alloy	Carbon	Silicon	Manganese
A	3.5	1.8	0.15
B	3.6	1.9	0
C	3.6	2.6	0

irons is applied to the simulation of the experimental results. The partition coefficients were evaluated by means of the Thermocalc software and the SGTE database,[22] which includes a previous assessment of the Fe-C-Si system.[23]

II. EXPERIMENTAL CHARACTERIZATION OF MICROSEGREGATIONS IN CAST IRON

A. *Experimental Details*

During a previous study,[24] a number of samples of alloy A in Table I were prepared by quenching during directional solidification (QDS). In such QDS experiments, a nearly constant cooling rate is imposed during the steady-state directional solidification before quenching. Transverse sections of these samples were used to study the evolution with temperature of the nodule count and the solid fraction at various cooling rates, between 17 and 72 K min^{-1}. Because of the hypoeutectic nature of the alloy under investigation, solidification proceeded in two steps, the proeutectic stage where austenite dendrites developed and the so-called eutectic reaction during which graphite nodules nucleated and grew, first freely and then encapsulated in an austenite shell. It was observed that new graphite nodules appeared continuously during the eutectic stage, but that there was a strong coupling between the nucleation phenomenon and the overall solidification process. Following this observation, a nucleation law was proposed [21] according to which the total number of nucleation sites is given by $N_V = A_n(\Delta T_L^g)^n$, where ΔT_L^g is the undercooling with respect to the graphite liquidus, and n and A_n are two constants characterizing the inoculation treatment. By considering that available sites for nucleation disappear with consumption of liquid, the number of nodules nucleated during a temperature change should be weighted by the volume of remaining liquid, V^1:

$$d(N_V) = n \cdot A_n \cdot (\Delta T_L^g)^{n-1} \cdot d\,(\Delta T_L^g) \cdot V^1$$

In the present study, the samples corresponding to the two extreme cooling rates investigated in the series of alloy A[24] were selected. The corresponding samples will be denoted A-1 and A-2 in the following. Two other QDS samples were prepared to get a fully white structure (sample B) and a mottled structure (sample C). The experimental conditions are summarized in Table II, where G stands for temperature gradient, V for withdrawal rate, and V_r for the average cooling rate in the mushy zone, calculated from the former data. The microstructure of samples B and C is illustrated in Figure 1. The volume fraction of austenite dendrites in sample B was about 30 pct, and the volume fraction of cementite in sample C was about 15 pct.

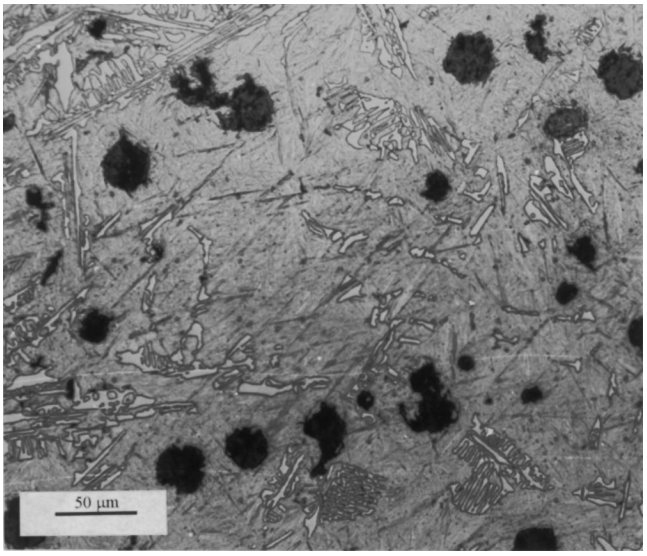

Fig. 1—Micrograph of sample C (mottled structure).

For microprobe analysis, one section of each of the samples was selected such that the corresponding temperature before quenching was slightly below the actual temperature for solidification completion. Microprobe analyses have been carried out using a CAMECA SX50 in spot mode under a 15 kV high voltage and with a beam regulated to 20 nA. The apparent content in each measured element, iron, silicon, and manganese, when any, was corrected for physical noise. The actual content was then calculated by using the correction program provided with the CAMECA instrument to account for absorption, atomic weight, and fluorescence effects. Each analysis consisted of measuring the elemental composition in points located on a predetermined square grid along which the sample was automatically displaced. The number of points and the size of the mesh depended on the analysis; they are indicated in Table III together with the counting time in each point. Two types of analysis were performed, denoted "map" when the mesh size was small with respect to the microstructure and "distribution" when it was large. The conditions used are summarized in Table III. Knowing the intensity of the X-ray signal of an element, it is possible to calculate the expected relative error on one measurement, which is assumed to be equal to ± 2 times the standard deviation. For a counting time of 20 seconds (samples A and B), it is 1.4 pct for iron, 3.4 pct for silicon, and 8 pct for manganese, while for a counting time of 40

Table II. Conditions Used in Quenching during Directional Solidification Experiments

Sample Reference	Microstructure	V (ms^{-1})	G (K m^{-1})	V_r (K s^{-1})	V_r (K min^{-1})
A-1	gray	$33.3 \cdot 10^{-6}$	8500	0.283	17
A-2	gray	$200 \cdot 10^{-6}$	7200	1.44	72
B	white	$300 \cdot 10^{-6}$	11,000	3.3	200
C	mottled	$300 \cdot 10^{-6}$	6000	1.8	109

Table III. Experimental Conditions Used for Microanalyses and Summary of Experimental Data

Type of Analysis	Sample	Number of Grid Points	Size of the Mesh (μm)	Counting Time (s)	f^{g}_{1} (Pct)	f^{g}_{2} (Pct)
Map	A-1	784	5	20	17.9	5.8
Map	A-2	2079	4	20	11.9	6.2
Distribution	A-1	676	40	20	5.3	5.8
Distribution	A-2	676	25	20	6.2	6.2
Distribution	B	900	50	20	0	0
Distribution	C	800	40	40	4.5	nm

nm: not measured.

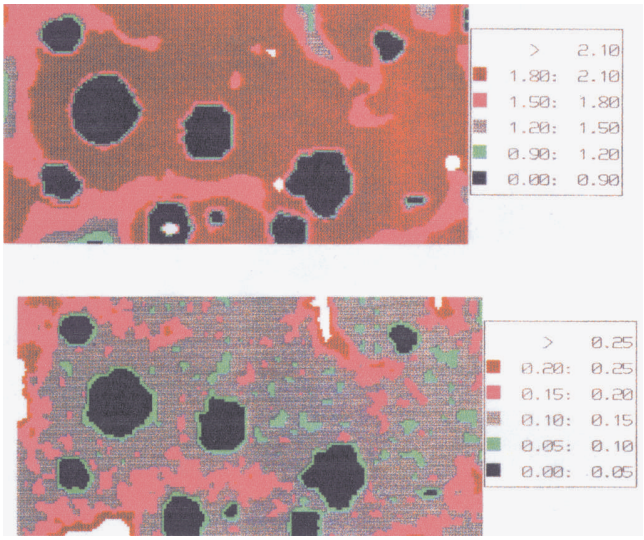

Fig. 2–Silicon (top) and manganese (bottom) maps recorded on sample A-1.

seconds (sample C), it is 1 pct for iron and 2.4 pct for silicon. For a more practical representation of the results, it appeared convenient to use the carbon content calculated by difference. For this element, the errors is the sum of the errors related to the other elements of the alloy under consideration.

B. *Silicon and Manganese Maps*

Use of an automatic microprobe analyzer allows drawing of precise maps of the distribution of elements within a given area. As an example, Figure 2 shows the map obtained for the silicon and manganese species on sample A-1. The graphite nodules are easily identified with their round shape and low silicon or manganese content, although one of them presents a small inoculant particle with very high silicon content in its center. Elongated areas with low silicon and high manganese contents are associated with last solidified zones in agreement with their partitioning behavior, which is negative for silicon and positive for manganese. In between, the graphite nodules and these latter zones, the compositional change of the quenched austenite is quite limited. Thus, maps give information on the sign of the microsegregation, as could line scans eventually give on its amplitude.

However, the main drawback of such map analysis is that the area on which measurements are made may be far too small to be representative of the entire sample. This is revealed in the present case by comparing the graphite surface fraction estimated from the microprobe analysis, f^{g}_{1}, to the value measured by image analysis, f^{g}_{2}, for the entire section of the sample. In the present case, estimate of f^{g}_{1} was obtained by considering that points with a iron content less than 50 wt pct were measurements made on graphite. From Table III, where these data are reported for samples A-1 and A-2, it is seen that the graphite fraction estimated from the map is greatly overestimated with respect to the value obtained by image analysis. It could have been underestimated as well if the maps were recorded in areas with a lower nodule count than the average.

C. *Distribution Analysis for Fully Graphitic SG Cast Iron*

In order to get a statistically better characterization of the chemical heterogeneities in the samples, it is necessary to investigate a larger area. This has been achieved by enlarging the mesh size of the grid, such that much more features of the microstructure could be investigated. The experimental conditions are given in Table III together with the related data under the specification ™distribution.∫ The relationship between the content in two different elements may be first investigated. Figures 3(a) and (b) show, respectively, the correlation between iron and silicon or manganese (Figure 3(a)) and between silicon and manganese (Figure 3(b)) in the case of sample A-1. In Figure 3(a), one may note the presence of one dense cloud of points for each of these elements at high iron content, both of which correspond to measurements made on the quenched austenite. A few points in the bottom left of the graph are related to the graphite phase, while the tail in between corresponds to measurements made close to the graphite/austenite interface. Again, the volume fraction of graphite was estimated as the ratio of the number of points with an iron content less than 50 pct. It is seen in Table III that the estimates of the graphite fraction thus obtained from distribution analyses, f^{g}_{1}, are much closer to the values measured by image analysis, f^{g}_{2}, than in the previous ™map∫ approach. This ascertains the representativity of the set of measurements performed by the distribution method.

In Figure 3(b), the set of points may be again divided in two parts: (1) a small cloud at low silicon and manganese contents related to measurements on graphite; and (2) a large cloud with a negative slope associated with measurements made on austenite. The slope of this latter cloud of points is negative because silicon and manganese segregate in an opposite way during solidification. Silicon content in austenite changes from a value close to the nominal content of

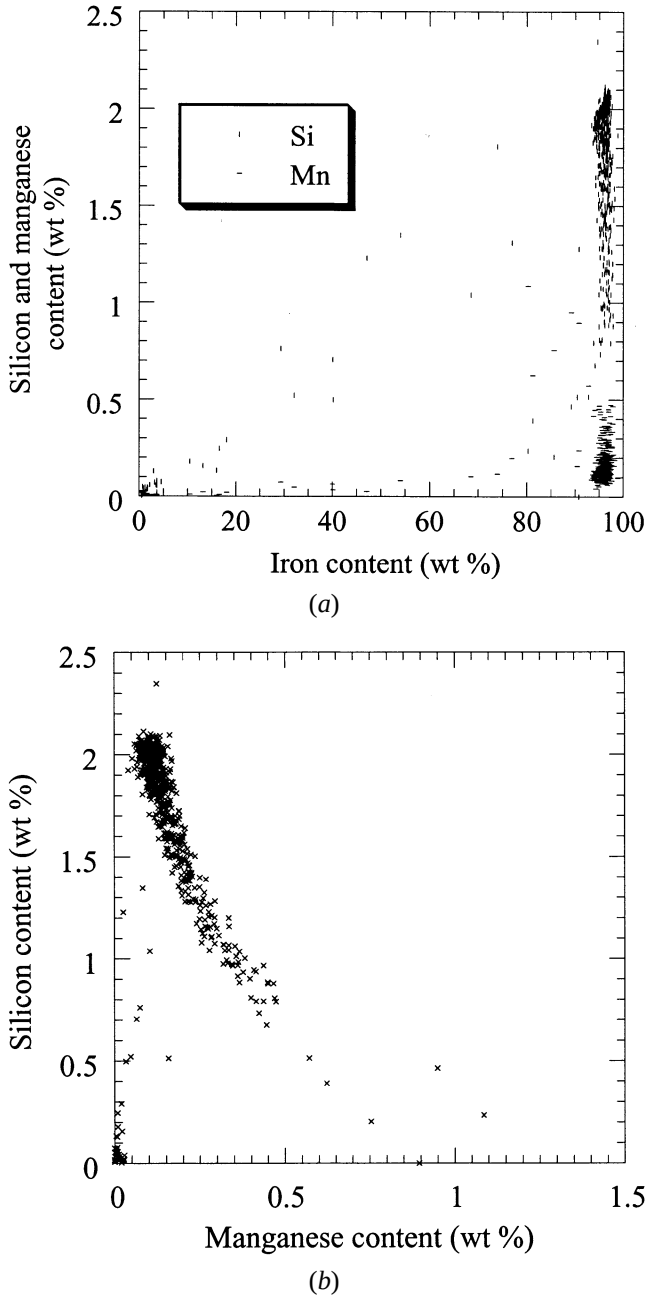

Fig. 3—Correlation between (*a*) silicon and manganese *vs* iron content and (*b*) manganese *vs* silicon measured by spot counting in the case of sample A-1.

the alloy to a value of about 0.7 wt pct, although a few measurements gave lower values. The manganese content in austenite increases from 0.1 to 0.45 wt pct, *i.e.*, about 3 times the nominal content.

In order to relate with the usual representation of the iron-rich corner of the Fe-C-Si phase diagram, the iron content was replaced by the carbon content, this latter being calculated by difference. In Figure 4(a), the points represent the carbon-silicon correlation obtained with the same measurements as in Figure 3a, when considering only countings with an iron content larger than 90 wt pct. In addition, the shaded area reported on the figure represents the expected scatter for one measurement, with its edges calculated as plus or minus the error estimated for the nominal composition of the alloy. It is thus seen that while the changes in carbon content are not significant, the measured silicon heterogeneities are quite pronounced and meaningful. The correlation is characterized by a cloud at the right part of the graph and a tail at the left part toward lower silicon contents. The same features were obtained with sample A-2. In agreement with the literature and the map analysis, the silicon content of the residual liquid, and thus of the austenite, decreases during the eutectic reaction: the tail at the left of the cloud may thus be associated with the end of the eutectic reaction. Accordingly, the cloud may thus be related to measurements made on the the off-eutectic austenite and the first austenite layers around the graphite nodules.

D. *Carbon versus Silicon Relationship for White and Mottled Cast Iron*

Figure 4(b) shows the carbon vs silicon relationship measured on a section of sample B, which exhibited a white eutectic structure. As before, the plot has been restricted to iron contents higher than 90 wt pct, and the figure has been complemented with a shaded area that corresponds to the estimated error domain associated with one measurement. The dense cloud of points with nearly constant silicon content related to primary austenite is found again, while the remaining features differ from those in Figure 4(a). A number of points are clustered at a composition that corresponds to cementite without silicon or at low silicon content, while most of the other measurements are in between these two clouds. There is, however, a trailing edge with silicon contents higher than the one corresponding to the primary austenite. These points are to be related to the solidification of the metastable eutectic with the associated buildup of a marked positive segregation of silicon.

The last analysis that has been carried out corresponds to the mottled structure obtained with sample C. Figure 4(c) shows the carbon *vs* silicon correlation for the section of this sample that was investigated. This figure presents features found for both fully graphitic and fully white structures: the dense cloud of points associated to the first austenite is surrounded by a tail on its two sides, toward both lower and higher silicon contents. A small cluster of points is related to cementite, with a few measurements lying in between this composition and austenite composition. From the comparison of the graphs in Figure 4, it is seen that microsegregations are more marked in white irons than in gray irons in the as-cast state in agreement with Feest *et al.*[12] However, it is possible that graphitizing heat treatments homogenize quite efficiently chemical heterogeneities related to redistribution of elements between cementite and austenite in ledeburite because of the very short distances involved in this case. After graphitization, segregations may thus be expected to be lower in initially mottled structures than in the two other cases. This could explain why malleable irons showed lower microsegregations than other irons.[2]

III. SIMULATION OF SOLIDIFICATION AND MICROSEGREGATION BUILDUP

The main features of the extension of the previous model[21] to account for segregation of substitutionnal solutes during solidification of SG cast irons are given in the Appendix, while the full derivation has been detailed elsewhere.[25]

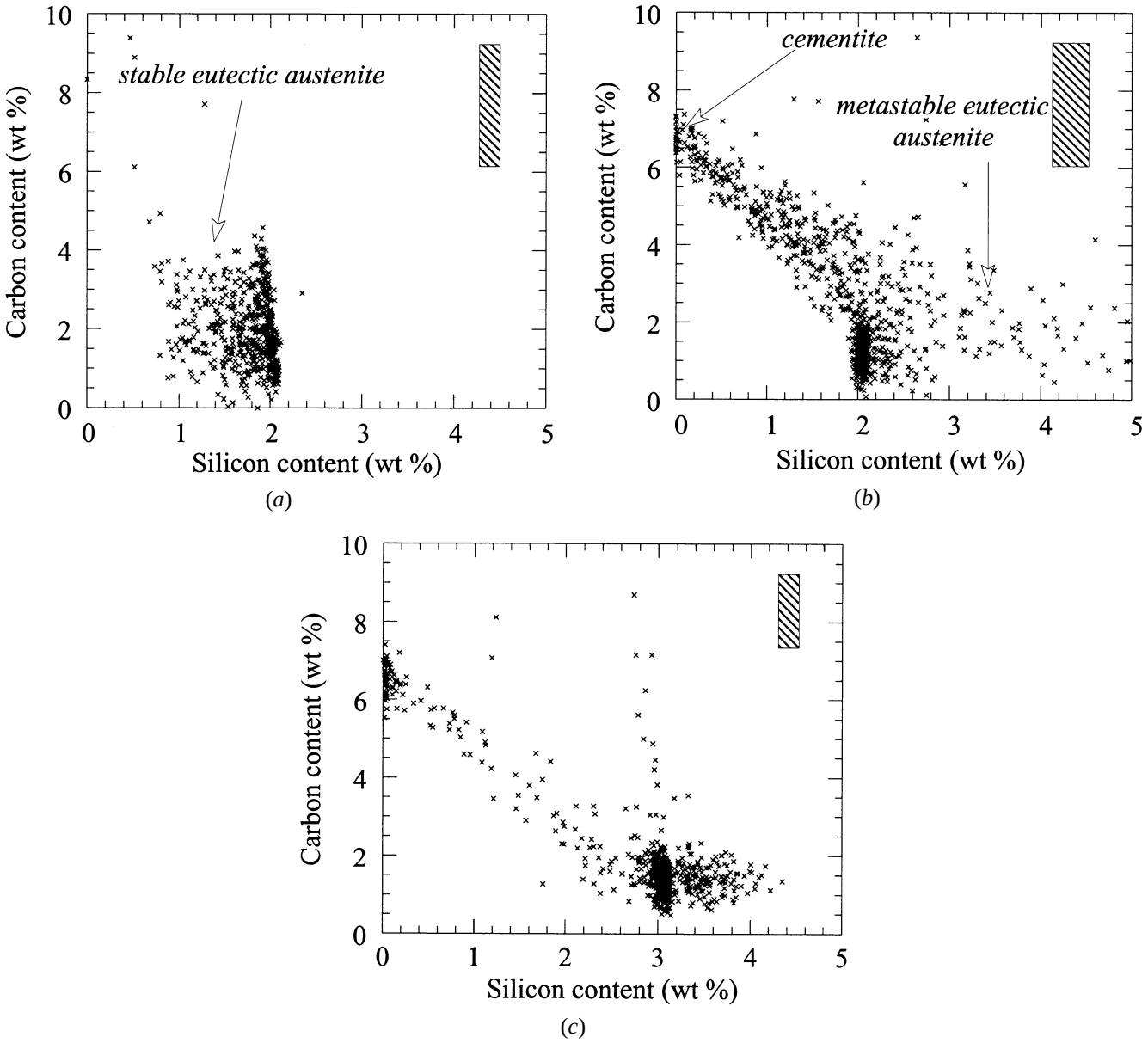

Fig. 4—Correlation between carbon *vs* silicon content in the case of sample (*a*) A-1, (*b*) B, and (*c*) C. The hatched areas represent the expected scatterband for each counting.

Data necessary for calculations, which were not given previously,[26] are given in this Appendix, where we also compare predicted solidification kinetics and nodule counts to experimental results obtained on alloy A.[24] It is worth emphasizing that solidification and nucleation kinetics predicted with the extended model are close to those obtained with the previous quasi-binary approach.[25] Therefore, the main interest of the present approach rests on the simulation of microsegregation buildup. Simulation of the four experiments listed in Table II was performed and the results are presented subsequently.

A. *Solidification in the Stable System (Samples A-1 and A-2)*

The calculated evolution of the silicon and manganese content of the remaining liquid and of the austenite that deposits during the solidification of sample A-1 *vs* temperature is shown in Figure 5. The solidification starts at the austenite liquidus and, as the temperature decreases, it is seen that the silicon and manganese contents of the liquid (solid lines in the figure), respectively, decrease and increase continuously. This is in agreement with the accepted segregation behavior of these species. The evolution of the austenite composition has been drawn with dotted lines in the figure. While the manganese contents of the austenite and liquid phases closely resemble each other it is worth noting that the silicon content of austenite first increases and then decreases. This is due to the strong sensitivity of the silicon partition coefficient with temperature and silicon content (Appendix): during the proeutectic stage, the change of the silicon content in the liquid is small and does not compensate for the increase of the silicon partition coefficient as the temperature drops; at the effective onset of the eutectic reaction, the volume

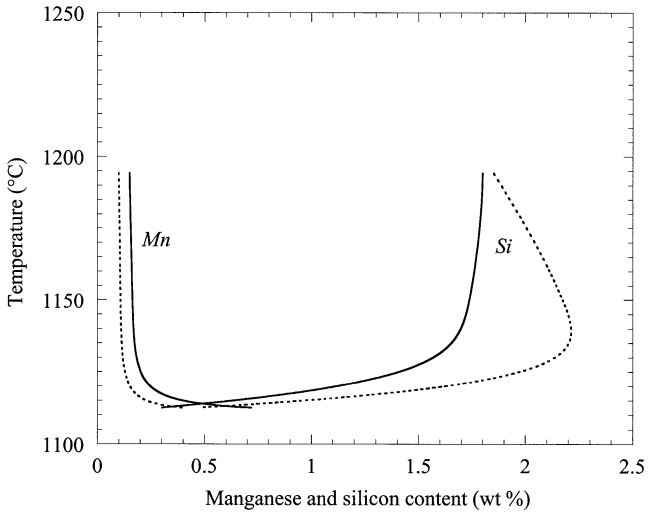

Fig. 5—Calculated evolution of the composition in manganese and silicon of the remaining liquid (solid line) and of the austenite, which deposits (dotted lines), in the case of sample A-1.

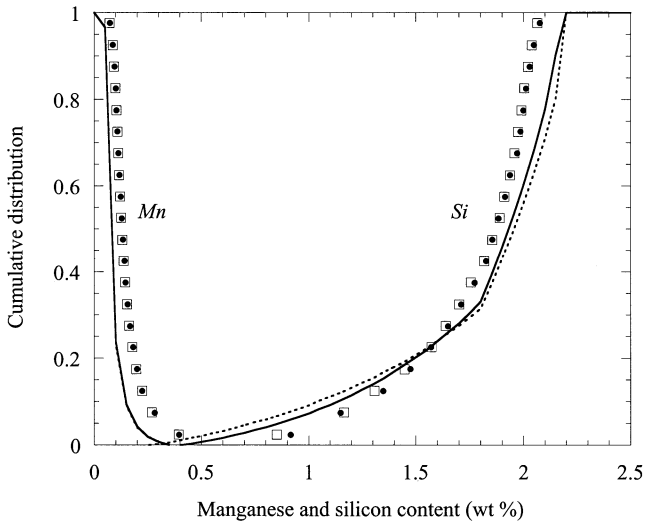

Fig. 6—Comparison of experimental (symbols) and calculated (lines) cumulative distributions of manganese and silicon in austenite in the case of samples A-1 (closed circles and solid lines) and A-2 (open squares and dotted lines).

solidified increases rapidly within a limited temperature range and the silicon content in the remaining liquid decreases dramatically and so does the silicon content of the austenite, which deposits. The change in the sign of the slope of the path followed by the austenite composition is thus related to the onset of the eutectic reaction. Interestingly enough, the predicted increase of the composition of the proeutectic austenite during cooling may explain the apparent positive segregation of silicon previously reported[2,11] in the case of high volume fraction of proeutectic (or off-eutectic) austenite.

Experimental as well as calculated data may be arranged to plot cumulative distribution of silicon and manganese in austenite. Concerning the experimental data, this has been made by considering that only the measurements with an iron content higher than 90 pct are representative of the austenite phase. The cumulative distributions have been obtained by sorting the data in ascending order in the case of silicon and in descending order in the case of manganese. Experimental and calculated distributions are compared in Figure 6 for samples A-1 and A-2. It is seen that the shape of the calculated distributions of both silicon and manganese agree fairly well with the experimental ones. The slight shift of the experimental manganese distribution curves to higher values with respect to the calculated ones is associated with the fact that the average measured content in this element is slightly higher than given by the chemical analysis. This could be due to some bias in the analysis system for these low contents. It is seen on this figure that there is no significant effect of the cooling rate in the range investigated, for both simulated and measured distributions. One should note, however, that the nodule count changed also slightly with the cooling rate. The expected effect of cooling rate and nodule count on the amplitude of silicon segregation has been further detailed elsewhere.[25]

B. *Solidification of White and Mottled SG Irons*

Calculations were then made accounting for the possibility of growth of the metastable eutectic. Ledeburite was

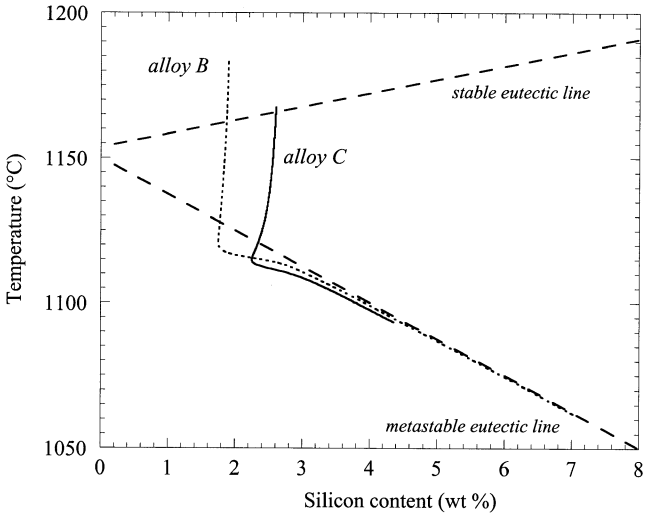

Fig. 7—Calculated evolution *vs* temperature of the silicon content in the remaining liquid for white (sample B) and mottled (sample C) solidification.

assumed to develop as spherical units, the growth law of which is given in the Appendix. The number of units could be varied, but was set equal to 10^2 mm^{-3} in all calculations. Figure 7 presents the evolution of the silicon content in the liquid *vs* temperature for experiments B and C. The stable and metastable eutectic lines are also plotted on the figure. For alloy C, the nucleation constants were set at the same values than for alloy A, while nucleation of graphite was not considered for alloy B. In the case of alloy B, the silicon content decreases slowly during the deposition of primary and off-eutectic austenite until the onset of the metastable eutectic reaction. After nucleation of white eutectic cells at the metastable eutectic temperature, their growth rate increases dramatically at an undercooling of about 10 °C. The solidification path then tends to stick to the metastable line and a strong positive segregation of silicon develops. For alloy C, the onset of the stable eutectic reaction appears

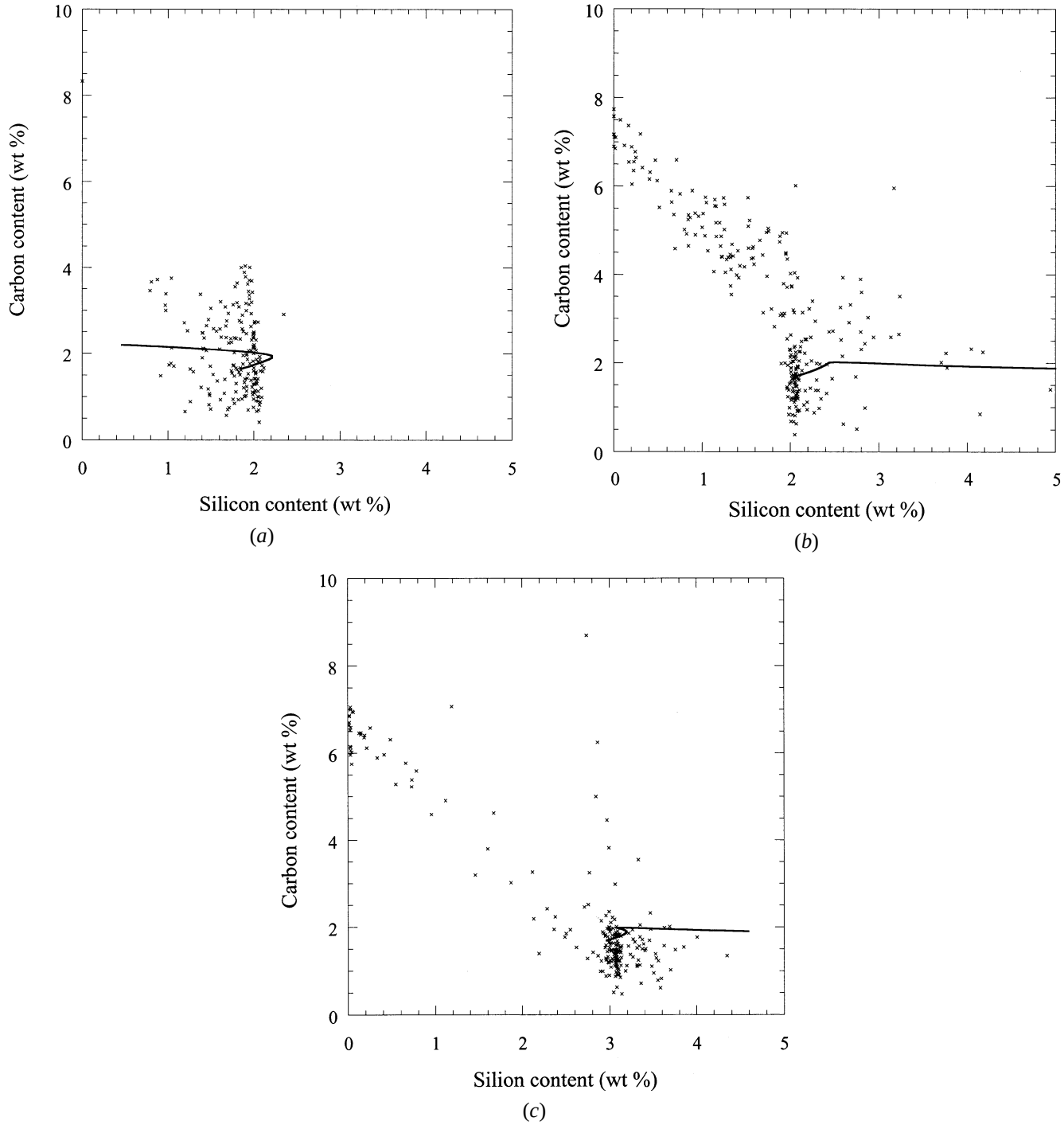

Fig. 8—Calculated correlation of silicon *vs* carbon content in the liquid and austenite which deposits for samples (*a*) A1, (*b*) B, and (*c*) C. Only 30 pct of the experimental points have been plotted to improve the clarity of the figure.

as an increased rate of silicon depletion at temperatures slightly above the gray to white transition. As previously shown, the metastable reaction leads to the development of a positive silicon segregation. However, the final silicon content in the liquid is higher in alloy B than in alloy C, because the amount of residual liquid at the stable to metastable transition was higher in the former alloy.

The predicted evolution of the composition of austenite which deposits has been drawn in Figure 8 for the same three samples as shown in Figure 4. Part (30 pct) of the experimental points have also been reported for comparison. It is seen that the calculated path of the austenite composition falls well within the related cloud of points. Although the details of the predicted compositional changes of austenite, cannot be evidenced from the experimental points on these figures, the amplitude of silicon microsegregation is conveniently reproduced. This is taken as an indication that the solidification paths are appropriately modeled.

IV. CONCLUSIONS

Experimental characterization of microsegregation in cast iron was made by means of point counting microanalysis

along a grid. The mesh size of the grid was chosen much larger than the characteristic size of the microstructure for statistical relevance. With this method, the differences of silicon distributions in alloys solidified in the stable system, the metastable system, or in both systems were clearly evidenced. Also, the distribution of manganese in alloys solidified in the stable system was investigated. By comparing these distributions to calculations, it was concluded that the solidification path of these alloys may be conveniently reproduced by means of predictions made with a physical model accounting for the nature of the alloy, either hypoeutectic or hypereutectic, and for the sensitivity to temperature and composition of the partition coefficient of alloying elements. This approach is being extended to the study of the segregation of minor elements such as copper, vanadium, *etc.*

APPENDIX

A. *Solidification in the Stable System*

The model developed to describe the buildup of microsegregation during solidification of SG cast irons makes use of a previous work where only carbon redistribution was accounted for.[21] The main hypotheses of the previous approach are maintained, and particularly the assumption that the eutectic reaction is controlled by carbon diffusion from the liquid to the graphite phase through the austenite shell surrounding the nodules. During the eutectic reaction, it is considered that the composition of the remaining liquid sticks to the metastable extrapolation of the austenite liquidus surface. The description of microsegregations is obtained by writing the mass balance equation for each of the alloying elements and coupling it to the previous set of equations.[25]

During the eutectic reaction in the stable system, the volume element that is considered contains one graphite nodule of radius r^g at its center, which grows inside an austenite shell of outer radius r^γ at time t, while the remaining volume, $V^{\text{off}} = \int_{r^\gamma}^{{}^t r^\gamma} 4\pi r^2\, dr$, is occupied by liquid and off-eutectic austenite. The term ${}^t r$ is the radius of the volume element at time t. Assuming that graphite is pure carbon and that the composition of the liquid is homogeneous, the mass balance of any substitutional solute i is written as

$$\rho^\gamma \int_{r^g}^{r^\gamma} 4 \cdot \pi \cdot w_i^\gamma \cdot r^2 \cdot dr + \rho^l (1 - g^\gamma) \cdot w_i^l \cdot V^{\text{off}} + \rho^\gamma \cdot g^\gamma \cdot \overline{w}_i^{\gamma,\text{off}} \cdot V^{\text{off}} = \rho^l \cdot {}^0w_i \cdot {}^0V \quad [A1]$$

where ${}^0w_i$, w_i^γ, and w_i^l are, respectively, the weight fraction of solute i in the alloy (nominal composition), in the austenite shell (depends on r), and in the liquid. The term $\overline{w}_i^{\gamma,\text{off}}$ is the average weight fraction of solute i in the off-eutectic austenite, ρ^ϕ is the density of phase ϕ (γ: austenite, l: liquid), ${}^0V$ is the initial volume of the volume element, and g^γ is the volume fraction of austenite in the off-eutectic volume V^{off}.

Considering that substitutional alloying solutes do not diffuse in solid phases, the variation with time of the i content in the eutectic austenite shell and in the off-eutectic austenite may be expressed as, respectively,

$$\frac{d}{dt}\int_{r^g}^{r^\gamma} w_i^\gamma\, 4\pi r^2 dr = 4\pi w_i^{\gamma/l}\,(r^\gamma)^2\,\frac{\partial r^\gamma}{\partial t} \text{ and}$$

$$\frac{d}{dt}\{g^\gamma V^{\text{off}}\,\overline{w}_i^{\gamma,\text{off}}\} = w_i^{\gamma/l}\,\frac{d}{dt}\{g^\gamma\, V^{\text{off}}\}$$

where $w_i^{\gamma/l}$ is the i content in austenite at the austenite/liquid interface and $\partial r^\gamma/\partial t$ is the rate of displacement of the austenite/liquid interface with respect to matter (the actual growth rate of the eutectic sphere with respect to the center of the volume element, dr^γ/dt, accounts for swelling due to graphite crystallization [21]).

Assuming finally that local equilibrium applies at the liquid/austenite interface, the time derivative of the mass balance for i species can be written after rearrangement:

$$w_i^l \cdot \frac{d\Phi_i}{dt} + \frac{\rho^l \cdot (1 - g^\gamma)}{\rho^l \cdot (1 - g^\gamma) + \rho^\gamma \cdot g^\gamma} \cdot \frac{dw_i^l}{dt} = -\frac{(k_i - \Phi_i) \cdot w_i^l \cdot \left[\rho^\gamma \cdot (r^\gamma)^2 \cdot \frac{dr^\gamma}{dt} - (\rho^\gamma - \rho^g) \cdot (r^g)^2 \cdot \frac{dr^g}{dt}\right]}{\rho^l \cdot \frac{({}^0r)^3}{3} - \rho^g \cdot \frac{(r^g)^3}{3} - \rho^\gamma \cdot \frac{(r^\gamma)^3 - (r^g)^3}{3}} \quad [A2]$$

with

$$\Phi_i = \frac{\rho^l \cdot (1 - g^\gamma) + \rho^\gamma \cdot k_i \cdot g^\gamma}{\rho^l \cdot (1 - g^\gamma) + \rho^\gamma \cdot g^\gamma} \text{ and}$$

$$\frac{d\Phi_i}{dt} = -\frac{\rho^l \cdot \rho^\gamma \cdot (1 - k_i)}{[\rho^l \cdot (1 - g^\gamma) + \rho^\gamma \cdot g^\gamma]^2} \cdot \frac{dg^\gamma}{dt}$$

where k_i denotes the equilibrium partition coefficient of the i solute between austenite and liquid.

The right-hand side of Equation [A2] may be calculated from the growth rates of the graphite nodule and austenite shell.[21] It should be emphasized that the assumption of no diffusion of substitutional alloying elements is realistic for the cooling rates encountered in usual solidification conditions, in agreement with recent calculations by Liu and Elliott.[19] The equation derived previously for the eutectic reaction may be used after appropriate simplifications to describe primary solidification in hypoeutectic alloy. In the case of hypereutectic alloys, it was considered that no segregations develop during primary deposition of graphite.[25]

B. *Overall Solidification Kinetics of Stable and Metastable Eutectics*

During primary deposition in hypoeutectic alloys, the overall solidification kinetics is the same in each volume element and does not need any special attention. In the case of hypereutectic alloys, one has to treat simultaneous nucleation and growth of the graphite nodules. This was described as in the previous work.[21] During the eutectic reaction, calculations consist of a nucleation step followed by a growth step. Nucleation is described exactly as in the case of the primary deposition of graphite, but it is assumed that any new nodule is immediately surrounded by an austenite shell to form a eutectic sphere. As in the previous work, the initial size ${}^0r^g$ of any new nodule is set to 3 μm and the initial depth of the austenite shell δr^γ to 1 μm. The set of nodules appeared at a given time-step generates a class of eutectic spheres, which have all the same geometric characteristics. Growth of the nodules and of the austenite shells is calculated for each class of eutectic spheres, according to the equations given earlier.[21] Impingement is taken into account by applying a correction factor to the growth laws as indicated previously.[26]

In addition, one may have to describe nucleation and

growth of cells of metastable eutectic when there is some remaining liquid at temperatures lower than the metastable eutectic temperature, T^w. It has been assumed that metastable eutectic cells appear instantaneously when this temperature is reached. These cells are assumed spherelike with a radius r^w, which varies according to the following growth rate law: $7 \times 10^{-7}\ (T^w - T)^2\ \mathrm{ms}^{-1}$.[27,28] Metastable eutectic cells are considered as a new phase and must be accounted for in the mass balances with a volume V^w. A new term is introduced in the total mass balance and in the mass balance of each solute j, either carbon or substitutional alloying element. This latter term is $\overline{w}_j^w V^w$, where $\overline{w}_j^w$ is the average j content of the metastable eutectic. The derivative of the solute balances is calculated as before if it is assumed that there is no compositional change of the previously deposited metastable eutectic, *i.e.*, $d(\overline{w}_j^w V^w) = w_j^{w*} dV^w$, where w_j^{w*} is the j content, which deposits.

The expression $V^{\mathrm{off}} = \dfrac{\rho^{l0} V - (\rho^g V^g + \rho^\gamma V^{\gamma,\mathrm{eut}} + \rho^w V^w)}{\rho^l (1 - g^\gamma) + \rho^\gamma g^\gamma}$, where $V^{\gamma,\mathrm{eut}}$ is the volume of austenite in the stable eutectic, is obtained from the total mass balance. Combining it with the derivative of the carbon balance leads to the following kinetics relation:[21]

$$-\left\{\Phi \cdot \frac{dw_{\mathrm{C}}^l}{dt} + w_{\mathrm{C}}^l \cdot \frac{d\Phi}{dt}\right\} = \frac{(1-\Phi)\cdot w_{\mathrm{C}}^l \cdot \rho^\gamma \cdot \dfrac{dV^{\mathrm{eut}}}{dt} + (w_{\mathrm{C}}^{w*} - \Phi \cdot w_{\mathrm{C}}^l)\cdot \rho^w \cdot \dfrac{dV^w}{dt}}{\rho^l \cdot {}^0V - \rho^g \cdot V^g - \rho^\gamma \cdot V^{\gamma,\mathrm{eut}} - \rho^w \cdot V^w} + \frac{(\rho^\gamma - \rho^g)\cdot [\Phi \cdot w_{\mathrm{C}}^l - w_{\mathrm{C}}^{\gamma/g} - w_{\mathrm{C}}^l \cdot (1 - k_{\mathrm{C}})]\dfrac{dV^g}{dt}}{\rho^l \cdot {}^0V - \rho^g \cdot V^g - \rho^\gamma \cdot V^{\gamma,\mathrm{eut}} - \rho^w \cdot V^w} + \frac{(\rho^\gamma - \rho^g)\cdot [\Phi \cdot w_{\mathrm{C}}^l - w_{\mathrm{C}}^{\gamma/g} - w_{\mathrm{C}}^l \cdot (1 - k_{\mathrm{C}})]\dfrac{dV^g}{dt}}{\rho^l \cdot {}^0V - \rho^g \cdot V^g - \rho^\gamma \cdot V^{\gamma,\mathrm{eut}} - \rho^w \cdot V^w} \quad [A3]$$

where V^{eut} is the volume of austenite in the eutectic sphere.

In the same way, one gets the following equation for any substitutional solute i:[25]

$$-\left\{\frac{\rho^l \cdot (1 - g^\gamma)}{\rho^l \cdot (1 - g^\gamma) + \rho^\gamma \cdot g^\gamma} \cdot \frac{dw_i^l}{dt} + w_i^l \cdot \frac{d\Phi_i}{dt}\right\} = \frac{(k_i - \Phi_i)\cdot w_i^l \left[\rho^\gamma \cdot \dfrac{dV^{\mathrm{eut}}}{dt} - (\rho^\gamma - \rho^g)\cdot \dfrac{dV^g}{dt}\right\}}{\rho^l \cdot {}^0V - \rho^g \cdot V^g - \rho^\gamma \cdot V^{\gamma,\mathrm{eut}} - \rho^w \cdot V^w} + \frac{\rho^w \cdot (w_i^{w*} - w_i^l \cdot \Phi_i)\cdot \dfrac{dV^w}{dt}}{\rho^l \cdot {}^0V - \rho^g \cdot V^g - \rho^\gamma \cdot V^{\gamma,\mathrm{eut}} - \rho^w \cdot V^w} \quad [A4]$$

The preceding equations can be easily combined to express the change of the solid fraction if the austenite liquidus may be expressed as an hyperplane in the composition space as proposed subsequently.

C. *Input Data*

All the thermophysical properties used in the previous studies[26] when considering SG cast iron as pseudobinary alloys have been used also in the present work. Only the data specific to the description of microsegregations are thus listed subsequently. It was considered that the austenite and graphite liquidus surfaces could be simply represented by planes, *i.e.*, that the austenite liquidus temperature, T_L^γ, and the graphite liquidus temperature, T_L^g, could be expressed by a linear relation of alloy composition. The following expressions were obtained from ternary diagram:[29]

$$T_L^\gamma = 1576.3 - 9730 \cdot w_{\mathrm{C}} + \sum_i m_i^\gamma \cdot w_i \text{ and}$$

$$T_L^g = -534.7 + 38910 \cdot w_{\mathrm{C}} + \sum_i m_i^g \cdot w_i$$

where m_i^γ and m_i^g are the austenite and graphite liquidus slopes relative to species i (their values are listed in Ref. 29), and w_i is the i content of the liquid.

The carbon partition coefficient was set equal to 0.47 as before, while a number of calculations were performed with the THERMOCALC software[22] to find the sensitivity to composition and temperature of the other partition coefficients of interest. The following expression for the silicon partition coefficient between austenite and liquid was finally found:

$$k_{\mathrm{Si}} = 1 + [0.0067(1200 - T)]\left[1 - \frac{w_{\mathrm{Si}}}{0.07}\right]$$

where T is the temperature expressed in Celsius. The value of k_{Si} is set to 1 when w_{Si} is larger than 0.07, which is approximately the composition of the ternary eutectic described previously.[22]

The manganese partition coefficient between austenite and liquid was expressed as

$$k_{\mathrm{Mn}} = 0.7 + 0.052(w_{\mathrm{Si}} - 2.5) - 0.008(w_{\mathrm{Si}} - 2.5)^2$$

where a slight dependence on w_{Si} is noted.

The silicon partition coefficient between cementite and liquid, $w_{\mathrm{Si}}^{w*}/w_{\mathrm{Si}}^l$, was set to zero.

D. *Solidification Kinetics and Nodule Nucleation during Stable Solidification*

Calculations were performed in order to simulate the solidification of samples of series A described earlier from an experimental point of view.[24] No account was made for the growth of the metastable eutectic since no cementite was observed in these experiments. Preliminary calculations showed that the only change that should be made with respect to the previous quasi-binary model is that the impingement factor should be set to $(V^l)^{0.5}$ in place of (V^l), where V^l is the volume fraction of remaining liquid. This change was considered in all calculations described in this article. The two constants of the nucleation law were set to $n = 3$ and $A_3 = 2 \times 10^{-3}\ \mathrm{mm}^{-3}\ \mathrm{K}^{-3}$.

In Figure 9, the calculated evolutions of the solid fraction (Figure 9(a)) and of the nodule count (Figure 9(b)) are drawn with dotted lines and compared to the experimental data plotted with symbols for the five cooling rates investigated. The experimental data are reported *vs* the temperature difference between the temperature of the dendrite tip and the temperature of the measurement section. In the calculations, the temperature of the start of solidification is the predicted liquidus temperature. In Figure 9(a), the calculated curves

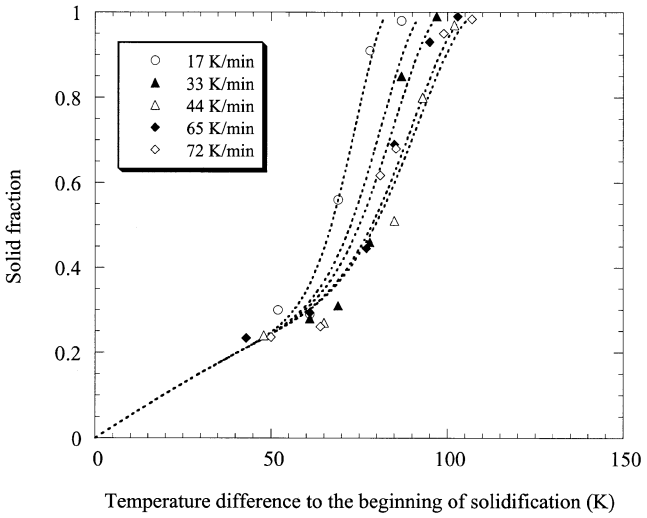

(*a*)

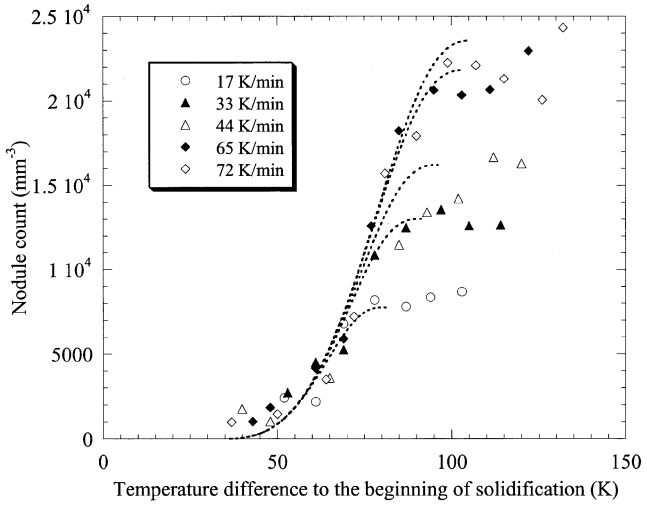

(*b*)

Fig. 9—Evolution (*a*) of the solid fraction and (*b*) of the nodule count during solidification of alloy A at various cooling rates (indicated in the figures). Symbols represent experimental data[24] and dotted lines calculations.

may be differentiated as the eutectic solidification is shifted to lower temperatures at increasing cooling rate. At the same time, it is observed that the eutectic temperature range is enlarged. In Figure 9(b), the differentiation of the calculated curves is also easily made as the final nodule count increases with the cooling rate. These features are well described by the simulation, and it is worth noting that the comparison of these two graphs illustrates the coupling between solidification and nucleation kinetics, which was mentionned previously. One may notice also that a number of measurements of the nodule count were performed on sections that wereentirely solid at the time of quenching. This was to check that the nodule count did not vary significantly after completion of solidification.

REFERENCES

1. J. Charbonnier and J.-C. Margerie: *Mém. Sci. Rev. Métall.*, 1967, vol. 64, pp. 345-57.
2. J. Charbonnier and J.-C. Margerie: in *Recent Research on Cast Iron*, H.D. Merchant, ed., Gordon and Breach Science Publishers, New York, NY, 1968, pp. 389-415.
3. G. Jolley and G.N.J. Gilbert: *Br. Foundryman*, 1967, pp. 79-92.
4. G. Jolley: in *The Solidification of Metals*, The Iron and Steel Institute of London, London, 1967, pp. 242-50.
5. N.K. Datta and N.N. Engel: *AFS Trans.*, 1976, vol. 83, pp. 431-36.
6. P.C. Liu and C.R. Loper: *AFS Trans.*, 1984, vol. 92, pp. 289-95.
7. J.-M. Schissler: *Hommes Fonderie* 1986, pp. 13-23.
8. K.L. Hayrinen, D.J. Moore, and K.B. Rundman: *AFS Trans.*, 1988, vol. 96, pp. 619-32.
9. R. Boeri and F. Weinberg: *Cast Met.*, 1993, vol. 6, pp. 153-58.
10. A. Owhadi, J. Hedjazi, P. Davami, M. Fazli, and J.M. Shabestari: *Mater. Sci. Technol.*, 1997, vol. 13, pp. 813-17.
11. N. Swindells and J. Burke: *Metall. Trans.*, 1971, vol. 2, pp. 3257-63.
12. E.A. Feest, G. McHugh, D.O. Morton, L.S. Welch, and I.A. Cook: *Solidification Technology in the Foundry and Casthouse*, The Metals Society, London, 1983, pp. 232-39.
13. J. Lacaze and G. Lesoult: *Mater. Sci. Eng.* 1993, vol. A173, pp. 119-22.
14. J. Lacaze and G. Lesoult: *Iron Steel Inst. Jpn. Int.*, 1995, vol. 35, pp. 658-64.
15. H. Fredriksson, J.T. Thorgrimsson, and I.L. Svensson: "State of the Art of Computer Simulation of Solidification and Casting," E-MRS, Les Editions de Physique, Les Ulis, France, 1986, pp. 267-75.
16. E. Lundbäck and I.L. Svensson: *Advanced Materials and Processes—EUROMAT'89*, DGM Informationsgesellschaftmbh Oberusel FRG, 1990, pp. 141-46.
17. L. Nastac and D.M. Stefanescu: *AFS Trans.*, 1993, vol. 134, pp. 933-38.
18. E. Fras, W. Kapturkievicz, and A.A. Burbielko: in *Modelling of Casting, Welding and Advanced Solidification Processes VII*, M. Cross and J. Campbell, eds., TMS, Warrendale, PA, 1995, pp. 679-86.
19. J. Liu and R. Elliott: *Mater. Sci. Technol.*, 1998, vol. 14, pp. 1127-31.
20. A. Kagawa and T. Okamoto: *J. Mater. Sci.* 1987, vol. 22, pp. 643-50.
21. G. Lesoult, M. Castro, and J. Lacaze: *Acta Mater.* 1998, vol. 46, pp. 983-95.
22. B. Sundman, B. Jansson, and J.O. Andersson: *CALPHAD*, 1985, vol. 9, p. 150.
23. J. Lacaze and B. Sundman: *Metall. Trans. A*, 1991, vol. 22A, pp. 2211-23.
24. J. Lacaze, M. Castro, N. Aichoun, and G. Lesoult: *Mém. Sci. Rev. Métall.*, 1989, pp. 85-97.
25. J. Lacaze: *Acta Mater.*, in press.
26. J. Lacaze, M. Castro, and G. Lesoult: *Acta Mater.*, 1998, vol. 47, pp. 3779-92.
27. R.A. Krivanek and C.E. Mobley: *AFS Trans.*, 1984, vol. 92, pp. 311.
28. L. Nastac and D.M. Stefanescu: in *Physical Metallurgy of Cast Iron V*, G. Lesoult and J. Lacaze, eds., Advanced Materials Research, SCITEC Publications, Switzerland, 1997, vols. 4–5, pp. 469-78.
29. M. Castro, M. Herrera, M.M. Cisneros, G. Lesoult, and J. Lacaze: *Int. Cast Met. Res. J.*, 1999, vol. 11, pp. 369-74.